Supplementary Information

Atomic Control of Active Site Ensembles in Ordered Alloys to Enhance Hydrogenation Selectivity

Anish Dasgupta[1†], Haoran He[1†], Rushi Gong[2], Shun-Li Shang[2] Eric K. Zimmerer[1], Randall J. Meyer[3], Zi-Kui Liu[2], Michael J. Janik[1,*] and Robert M. Rioux[1,4,*]

[1]Department of Chemical Engineering, The Pennsylvania State University, University Park, PA 16802, USA

[2]Department of Materials Science and Engineering, The Pennsylvania State University, University Park, PA 16802, USA

[3]ExxonMobil Research and Engineering, Annandale, NJ 08801, USA

[4]Department of Chemistry, The Pennsylvania State University, University Park, PA 16802, USA

[*]Corresponding Author.

[†]Equal Contribution.

Table of Contents

S1: Four symmetry inequivalent site of the γ-brass phase

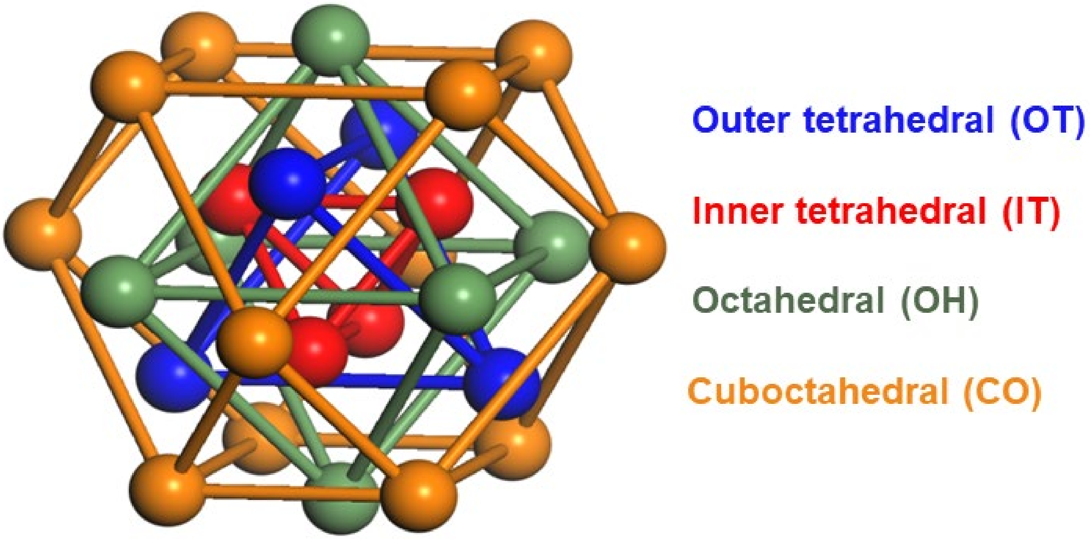

Figure S1. γ-brass structure with four symmetry inequivalent positions.[1]

S2: Materials and Experimental Methods

S2.1 Synthesis of γ-brass phase Pd-Zn Materials

The γ-brass phase materials were synthesized using a common bulk diffusion technique.[2-6]. An appropriate amount of Pd powder (Alfa Aesar, 99.99%) and Zn granules (Sigma Aldrich, 99.99%) were loaded into an alumina crucible (LSP ceramics). The crucible was placed in a home-made quartz ampoule, evacuated to a pressure of ~30 mTorr and flame-sealed under vacuum. The ampoule was heated in a box furnace at 700°C for 30 h. The resultant ingot was recovered by breaking the ampoule and then crushed to a powder in a Spex SamplePrep 8000 series ball mill. The stainless-steel vessel used during ball milling was loaded inside a nitrogen purged glovebox and about 4 mL Vertrel XF (Dupont) was used as a fluidizing medium. After crushing, the samples were once again annealed under vacuum at 500°C for 7 days to ensure the materials returned to their thermodynamically favored configuration which may have been perturbed during the high energy ball milling.

S2.2 Synthesis of γ-brass Pd-M-Zn Materials

The approach to synthesize the ternary γ-brass phases was identical to the one described above. The starting composition now included the stoichiometric amount of Au (Alfa Aesar, 99.99%), Ag (Sigma Aldrich, 99.99%) or Cu (Sigma Aldrich, 99.99%) in addition to Pd and Zn. The temperature program was also slightly different and consistent with Thimmaiah et al.[7] The temperature was raised to 800°C for 20 h and held at that temperature for 92 h. It was then cooled to 500°C for 8 h and then to room temperature by shutting off the furnace.

S2.3 Elemental Analysis of Pd-(M)-Zn Materials

The composition of the synthesized γ-brass materials were confirmed through two independent techniques—ICP-OES and SEM-EDS. The ICP-OES experiments were performed on an Agilent Technologies 700 series ICP-OES. Approximately 10 mg of each sample was first dissolved in 4 ml freshly prepared aqua regia or concentrated HNO_3 and then diluted to 16 ml by the addition of DI water. The instrument was calibrated using solutions of appropriate concentrations prepared by diluting Pd, Zn or coinage metal standards (1mg/mL, High Purity Standards) with DI water. SEM-EDS data was collected on a Zeiss-Sigma FESEM. A small amount of each sample was loaded on aluminum mounts and held in place by double sided adhesive carbon tape. A 9 × 9 carousel sample holder was used to load the samples into the instrument chamber for analysis.

S2.4 BET Surface Area

BET surface area was determined by using ~150 mg of each sample in a Micromeritics 3-Flex instrument. N_2 was used as the probe molecule while the system was kept at the normal boiling point of N_2 (~77 K).

S2.5 X-ray Diffraction

X-ray diffraction (XRD) for Rietveld refinement was performed on a PANalytical X'pert Pro instrument using constant wavelength Cu K_α radiation. A graphite monochromator was used on the detector side to cut off K_β peaks which can interfere with Rietveld refinement. The incident side optics had 1/2° anti-scatter slits, 10 mm beam mask, 1/4° fixed divergence slits and 0.04 rad soller slits. A NIST 640d standard (silicon) was used to determine the instrument parameter file for Rietveld refinement (using the EXPGUI interface of the General Structure Analysis System (GSAS) software package). A silicon zero-background holder was used in all measurements to eliminate background signal. Diffraction data was collected in the 2θ range 10-90°. XRD for phase identification purposes was performed either on the X'Pert Pro or a PANalytical Empyrean using similar optical settings as described above with the exception that a Ni β-filter was used in place of the monochromator.

S2.6 Ethylene Hydrogenation on Pd-Zn γ-brass Catalysts

Pd-Zn catalysts (~200 mg) were loaded in a fritted glass tube (10 mm ID, ChemGlass) which operates as a plug-flow reactor. The total flow rate was ~34 mL/min with 5 Torr ethylene (Praxair, 10% ethylene in He), 200 Torr hydrogen (ultra high purity (UHP), Praxair) and balance He (UHP, Praxair). The reactor was placed inside a custom designed clam-shell furnace fitted with a K-type thermocouple (Applied Test Systems). A temperature range of 34-55°C was used. Catalysts were reduced for 8 h at 250°C in hydrogen and then held for 20 min at that temperature under He flow before being cooled under He flow to the desired reaction temperature. At least 30 min was provided for the catalyst to equilibrate at the reaction temperature before starting the flow of reactants. The product stream was analyzed with an online Hewlett Packard 5890 Series II GC. All conversions were within 10% and may be considered differential.

S2.7 Acetylene Hydrogenation

Acetylene hydrogenation was performed in a similar set up to the one discussed above with the exception than an Agilent 7890A GC was used for effluent analysis. 150 mg Pd_8Zn_{44}, 0.4 mg Pd_9Zn_{43} diluted in 9.6 mg SiO_2 (10 mg sample from a well-mixed 4% Pd_9Zn_{43} in SiO_2), 0.3 mg $Pd_{10}Zn_{42}$ diluted in 9.7 mg SiO_2 (10 mg sample from a well-mixed 3% $Pd_{10}Zn_{43}$ in SiO_2), 15-20 mg each of Pd_8AuZn_{43}, $Pd_8Ag_3Zn_{41}$ and $Pd_8Cu_3Zn_{41}$ and a 2 × 2 mm^2 Pd foil (Sigma Aldrich) in a 60 mg SiO_2 bed were used as catalysts for the reaction. Each catalyst was reduced for 4 h at 250°C by flowing hydrogen and then held for 20 min under He flow before each experiment. The reactants were 2.2 Torr acetylene (Praxair, 1% acetylene in He), 220 Torr hydrogen and balance He at a total flow rate of 32 mL/min. The reaction temperature was 160°C. Selectivity of any product P (having N_P carbon atoms per molecule) is measured as:

$$S_P = \frac{N_P}{2}\frac{(P)_{t=t} - (P)_{t=0}}{(C_2H_2)_{t=0} - (C_2H_2)_{t=t}} \qquad (1)$$

Normalized activity of the catalyst is calculated as:

$$Activity = \left(\frac{(C_2H_2)_{t=0} - (C_2H_2)_{t=t}}{(C_2H_2)_{t=0}}\right) * \frac{1}{(surface\ area) * (wt.frac.Pd)} \qquad (2)$$

S2.8 Competitive Acetylene-Ethylene Hydrogenation

Competitive acetylene and ethylene hydrogenation were performed in a home-made batch reactor similar to that used by Spanjers et al.[5] The reactor tube had an outer diameter of 5 mm. The batch reactor was evacuated to 180 mTorr before filling with reactant gases. The catalyst was initially reduced for 4 h at 250°C by evacuating the set-up and back-filling to ~850 Torr hydrogen. It was then cooled to room temperature, evacuated, and filled with 550 Torr 1% acetylene, 170 Torr $^{13}C_2$-ethylene (99%, Sigma Aldrich), 100 Torr hydrogen (UHP, Praxair) and 20 Torr Ar (UHP, Praxair). The materials were found to be inactive at room temperature and a minimum of 2 reference data points were taken under this “initial condition” before heating to a reaction temperature of 160°C. Periodic manual sampling was performed using a 100 µL gas-tight syringe (Hamilton Company) and the products analyzed with a Shimadzu 2010 QP Ultra GC-MS. The Ar signal (m/*z* = 40) was used as an internal standard to correct for fluctuations in sample injection volume. The ethane and ethylene isotopomer distribution was determined using the matrix method of Price and Iglesia[8] which has been previously utilized for distinguishing between ^{12}C and ^{13}C

compounds by Bui and Bahn[9] and Spanjers et al.[5,10] The intrinsic selectivity of all species were calculated using the equation for S_p (eqn 1). In the intrinsic selectivity calculation for ethylene and ethane, only the ^{12}C component was used for ethylene and ethane. For the net selectivity to ethylene, both the ^{12}C fraction from acetylene and the remaining ^{13}C fraction from labeled ethylene was considered. The net ethylene selectivity is calculated as:

$$\left(S_{C_2H_4}\right)_{net} = \frac{{}^{12}C_2H_4 - {}^{13}C_2H_6}{(C_2H_2)_{t=0} - (C_2H_2)_{t=t}} \qquad (3)$$

Table S1. BET surface area and elemental analysis of Pd-Zn catalysts

Sample	**Elemental Analysis**		**BET Surface Area (m^2/g)**
	ICP	**SEM-EDS**	
Pd_8Zn_{44}	$Pd_{7.8}Zn_{44.2}$	Pd_8Zn_{44}	1.29 ± 0.19
Pd_9Zn_{43}	$Pd_{9.2}Zn_{42.8}$	$Pd_{8.9}Zn_{43.1}$	0.85 ± 0.09
$Pd_{10}Zn_{42}$	$Pd_{10.1}Zn_{41.9}$	$Pd_{10.3}Zn_{41.7}$	0.94 ± 0.05
Pd_8AuZn_{43}	$Pd_{7.9}Au_{1.3}Zn_{42.8}$	$Pd_8Au_{1.2}Zn_{42.8}$	1.40 ± 0.05
$Pd_8Ag_3Zn_{41}$	$Pd_{8.2}Ag_{3.3}Zn_{40.5}$	$Pd_{8.5}Ag_{3.5}Zn_{40}$	1.61 ± 0.01
$Pd_8Cu_3Zn_{41}$	$Pd_{8.2}Cu_{3.1}Zn_{40.7}$	$Pd_8Cu_{2.8}Zn_{41.2}$	1.46 ± 0.06

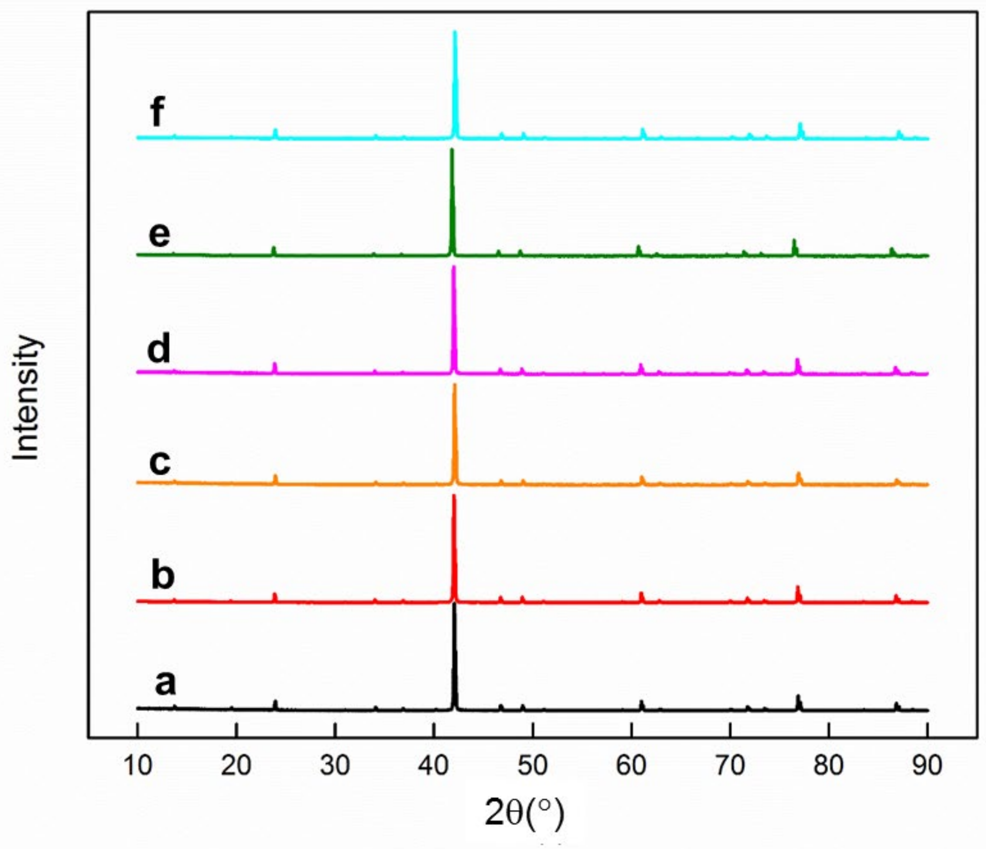

Figure S2. X-ray diffractograms of (a) Pd_8Zn_{44}, (b) Pd_9Zn_{43}, (c) $Pd_{10}Zn_{42}$, (d) Pd_8AuZn_{43}, (e) $Pd_8Ag_3Zn_{41}$ and (f) $Pd_8Cu_3Zn_{41}$. All sharp features can be indexed to the cubic γ-brass phase with space group $I\bar{4}3m$.

S3: Rietveld Refinement Results

S3.1: Rietveld Refinement of Pd-Zn γ-brass Materials

Rietveld refinement of the Pd-Zn γ-brass phase XRD patterns were performed using the GSAS interface and consistent with a method we previously used to identify site occupation factors in the Ni-Zn γ-brass phase.[1] It is briefly discussed below:

For Pd_8Zn_{44}, we constructed four models by placing the 8 Pd atoms in any one of the IT, OT, OH or CO site. For IT or OT (multiplicity = 8) this corresponds to a site occupation factor (SOF) = 1 and thus no further constraints are implemented. For OH (multiplicity = 12) and CO (multiplicity = 24) this leads to SOF of 0.67 and 0.33 respectively. Thus these were modeled as shared site (Pd + Zn) with the total SOF = 1. No refinement of SOF was performed. For shared sites, the thermal factor as well as the lattice coordinates are constrained to be identical for both Pd and Zn. These constraints have been employed for all refinements mentioned here-in whenever shared sites are modeled. It was found that statistically the best fit was obtained when Pd occupied the OT site. To further confirm the preference of Pd to occupy the OT site we then allowed the SOF of the Pd containing site in the above-mentioned models to vary. The SOF refined to negative values on IT and CO sites thus proving the absence of Pd from those positions. On the OH site, the Pd SOF refined to 0.803 leading to a stoichiometry of $Pd_{9.64}Zn_{42.36}$ which is far removed from the elemental composition determined through SEM-EDS and ICP-OES. Finally, for the model with Pd on the OT site the SOF refined to 0.97 leading to a close match in stoichiometry as determined through SEM-EDS and ICP-OES. Further, this model was statistically the best fit of all the models and practically equal to the model with Pd SOF = 1 on the OT site mentioned above. In Table S2, we present this latter model as it achieves an equally good fit with fewer parameters but there is no discernible difference between the models with Pd on OT site irrespective of if the SOF can refine or not (fixed at 1).

For Pd_9Zn_{43} and $Pd_{10}Zn_{42}$ it was assumed the first 8 Pd atoms continue to occupy the OT site and effort was solely focused towards identifying the location of the 1 (or 2) excess Pd atom(s) per unit cell. Four models were tested with the excess Pd atom(s) on any one of the IT, OH or CO site or distributed over all three. It was observed the best fit cannot be determined by any statistical measure because differences in intensities are very small when the position of only one or two atoms vary between models. We employed our independent knowledge of sample stoichiometry (known from ICP and SEM-EDS) to identify the best model. In both cases the best match was obtained when the excess Pd atom(s) were on the OH site. The full refinement results are presented in Table S2.

Table S2. Lattice parameters, fractional atomic coordinates, site occupation factors (SOF), isotropic displacement parameters (U_{iso}), and fit parameters for the refined powder X-ray diffraction data for Pd_8Zn_{44}, Pd_9Zn_{43}, and $Pd_{10}Zn_{42}$.

Site[a]	element	parameter	Pd_8Zn_{44}	Pd_9Zn_{43}	$Pd_{10}Zn_{42}$
		a (Å)	9.1051 ± 0.0005	9.1038 ± 0.0007	9.1015 ± 0.0005
		χ^2	2.61	2.36	3.55
		$R_{F\^2}$	0.085	0.1154	0.056
IT(8)	Zn	*x=y=z=*	0.1077 ± 0.0004	0.1081 ± 0.0006	0.1083 ± 0.0005
		SOF	1	1	1
		U_{iso}	0.028	0.021	0.027
OT(8)	Pd	*x=y=z=*	-0.1734 ± 0.0003	-0.1739 ± 0.0003	-0.1733 ± 0.0003
		SOF	1	1	1
		U_{iso}	0.023	0.021	0.028
OH(12)		*y=z=0; x=*	0.356195 ± 0.0005	0.3572 ± 0.0006	0.3574 ± 0.0005
		U_{iso}	0.016	0.012	0.010
	Zn	*SOF*	1	0.93 ± 0.034	0.83 ± 0.027
	Pd	*SOF*	0	0.07 ± 0.034	0.17 ± 0.027
CO(24)	Zn	*x=y=*	0.3108 ± 0.0004	0.3115 ± 0.0005	0.3113 ± 0.0004
		z=	0.0390 ± 0.0005	0.0382 ± 0.0006	0.0385 ± 0.0005
		SOF	1	1	1
		U_{iso}	0.025	0.022	0.023

[a] Quantity in parenthesis represents the multiplicity of each Wyckoff position site in the unit cell with space group $I\bar{4}3m$. See details in Table S7.

S3.2: Rietveld Refinement of Pd_8AuZn_{43}

Several different cases are tested to identify the site preference of Pd and Au while Zn is fixed on all sites which are not explicitly refined. In the first case, Pd and Au are refined on the OT site while Pd and Zn are refined on the OH site but the Au SOF refines to 0 indicating Au does not displace Pd from the OT site. In the second case, all 8 Pd atoms are fixed on the OT site and Au and Zn are refined on the OH site. The Au SOF refines to 0.084 in excellent agreement with the nominal stoichiometry ($12 \times 0.084 = 1$). We attempted a third case where Pd is once again fixed on the OT site and Au and Zn are refined on all other sites. The Au SOFs on IT and CO sites are ~0 while the SOF on the OH site is once again 0.084. The refinement results of the best fit case (second case discussed above) are presented in Table S3.

Table S3. Rietveld refinement fitting parameters for Pd_8AuZn_{43} X-ray diffractogram.

a = 9.111220±0.000429, X^2 = 3.390, wR_p = 0.1082, R_p= 0.0711, R_{F^2} = 0.0783.

Site	x	y	z	SOF	U_{iso}
OT	-0.173644±0.00029	= x	= x	Pd 1	0.0258
IT	0.107924±0.00054	= x	= x	Zn 1	0.032
OH	0.358271±0.00048	0	0	Au 0.084±0.011 Zn 0.917±0.011	0.0164
CO	0.310321±0.00045	= x	0.039527±0.00053	Zn 1	0.0284

S4: Computational (DFT) Methods

All DFT calculations were performed using Vienna Ab Initio Simulation Package (VASP).[11-13] The Perdew−Burke−Ernzerhoff (PBE) generalized gradient approximation was applied with a plane wave basis set with energy cutoff of 450 eV.[14] The Methfessel-Paxton (MP) smearing method was applied in all calculations with a broadening value of 0.2 eV.[15] Structural optimizations were carried out until forces on all atoms were less than 0.05 eV/Å. A 6 × 6 × 6 Monkhorst−Pack K-point mesh sampling was used for bulk (Pd_8Zn_{44}, Pd_9Zn_{43}, $Pd_{10}Zn_{42}$, Pd_8AgZn_{43}, Pd_8CuZn_{43} and Pd_8AuZn_{43}) optimization.[16] During bulk optimization, 8 Pd atoms were placed in OT sites, which has been experimentally established; therefore, Pd_8Zn_{44} has a single structure that matches site occupancies.[2] To identify the energetically most favorable site occupancies in bulk Pd_9Zn_{43}, we performed structural and lattice optimization placing the 9th Pd atom in Pd_9Zn_{43} in either an OH, IT or CO site. The two additional Pd atoms in $Pd_{10}Zn_{42}$ were placed in OH, IT, CO or a combination of two different sites. For both Pd_9Zn_{43} and $Pd_{10}Zn_{42}$, we assumed the 8 OT sites remained occupied by Pd atoms. For Pd_8AuZn_{43}, Pd_8AgZn_{43}, and Pd_8CuZn_{43}, we considered all possible symmetry non-equivalent structures with the Au, Ag or Cu atom occupying OT, OH, IT or CO sites and Pd atoms in OT and OH sites. We assumed all 8 OT sites remained occupied by either Pd or Au. A reduced 2 × 2 × 2 Monkhorst−Pack k-points mesh was used to screen site occupancies followed by a 6 × 6 × 6 Monkhorst−Pack k-point mesh for final optimization of preferred structures. A subset of structures was tested with both k-point meshes to verify that the lower density sampling captured the energetic order of different metal atom distributions.

Four mirrored surface slabs with Miller indices (111), (100), (110), ($1\bar{1}0$) were built from Pd_8Zn_{44}, Pd_9Zn_{43}, $Pd_{10}Zn_{42}$, Pd_8AuZn_{43}, Pd_8AgZn_{43} and Pd_8CuZn_{43}. A 6 × 6 × 1 Monkhorst−Pack k-point mesh sampling was used for surface calculations. Due to non-identical stoichiometry between surface slab and bulk, subtraction of bulk energies of Pd for Pd_8Zn_{44} and Pd and M (M = Au, Ag, Cu) for Pd_8MZn_{43} were used to calculate surface energies, as:

$$f(Pd_8Zn_{44})^{bulk} + xPd^{bulk} \xrightarrow{yields} (Pd_{x+8*f}Zn_{44*f})^{surface} \tag{4}$$

$$E^{surface} = \frac{[E^{Pd_{x+8*f}Zn_{44*f}} - f(E^{Pd_8Zn_{44}}) - x(E^{Pd})]}{2A} \tag{5}$$

$$f(Pd_8MZn_{43})^{bulk} + xPd^{bulk} + yM^{bulk} \xrightarrow{yields} (Pd_{x+8*f}M_{y+f}Zn_{43*f})^{surface} \tag{6}$$

$$E^{surface} = \frac{[E^{Pd_{x+8*f}M_{y+f}Zn_{43*f}} - f(E^{Pd_8MZn_{43}}) - x(E^{Pd}) - y(E^{M})]}{2A} \tag{7}$$

Wulff surfaces were constructed using the open source program Wulffmaker,[17] which has been successfully used by a number of researchers to determine equilibrium particle shapes.[1,18-21]

The binding energy for surface species was calculated as:

$$\Delta E_{ads} = E_{slab+i} - E_{slab} - E_i \tag{8}$$

where E_{slab+i}, E_{slab}, and E_i are the total electronic energies of the metal–adsorbate system, the metal slab, and the adsorbed species in the gas phase, respectively. The nudged elastic band (NEB) method was applied to locate transition states, and each transition state was verified through the existence of a single imaginary vibrational frequency.[22]

S5: DFT Bulk Calculations

DFT calculations provide theoretical confirmation of the XRD results in predicting the site occupancies of the excess (>8) Pd atom(s) in Pd_9Zn_{43} and $Pd_{10}Zn_{42}$. Agreement between XRD and DFT in site occupancies helps to validate the DFT approach for consideration of stable surface structures. For Pd_9Zn_{43}, the additional Pd atom was placed in OH, IT or CO sites. The relative bulk energies are shown in Figure S3. The energetically favorable structure has 8 Pd atoms in OT sites and the 9th Pd in an OH site, which agrees with XRD. DFT results show a sizable energetic preference for this occupancy.

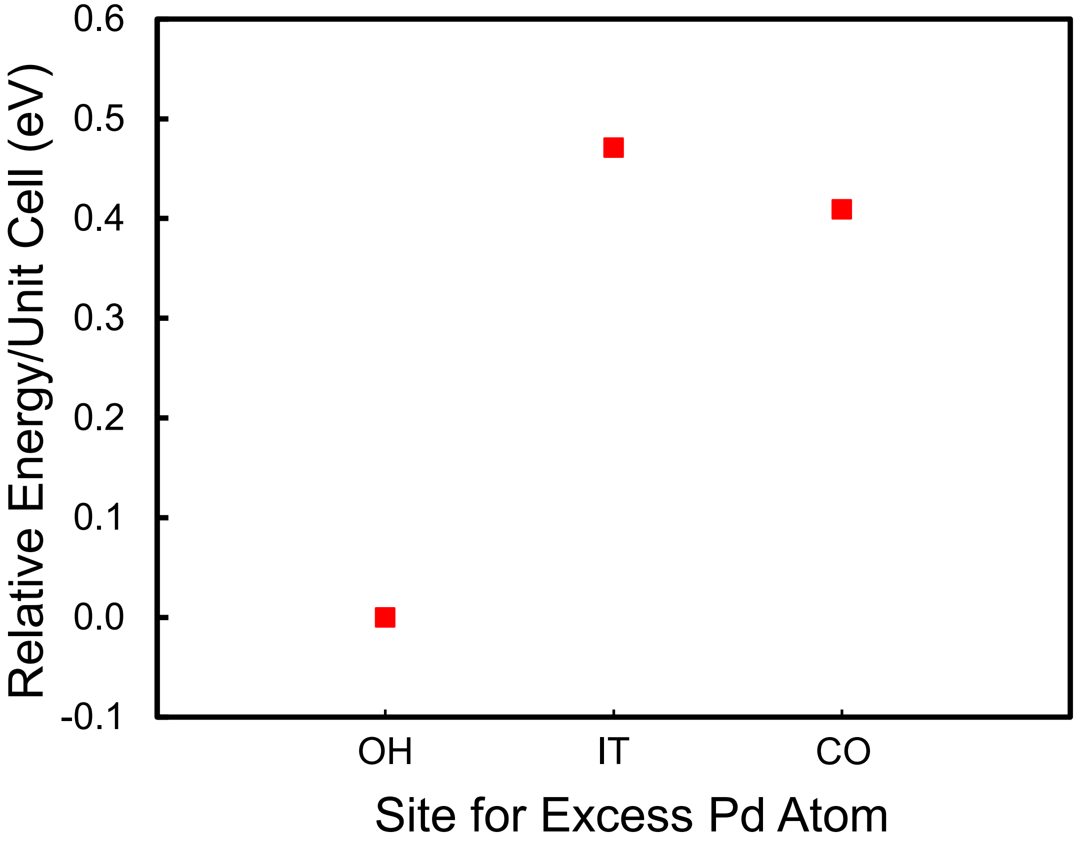

Figure S3. Pd_9Zn_{43} relative DFT energies with the 8 Pd atoms in OT site and additional Pd in OH, IT or CO sites.

For $Pd_{10}Zn_{42}$, the two excess Pd atoms can occupy OH-OH, OH-IT, OH-CO, IT-IT, CO-CO and IT-CO sites. Figure S4 summarizes energies of all $Pd_{10}Zn_{42}$ bulk structures referenced to the most stable structure, which can be obtained by placing 8 Pd atoms in OT sites and 2 Pd in OH sites, in good agreement with experimental results discussed above. With the extra 2 Pd atoms in OH sites, there are 5 unique structures due to difference in distance between the two extra Pd atoms. Only the lowest energy structure exposes two trimers on the $(1\bar{1}0)$ surface, as shown in Table S4.

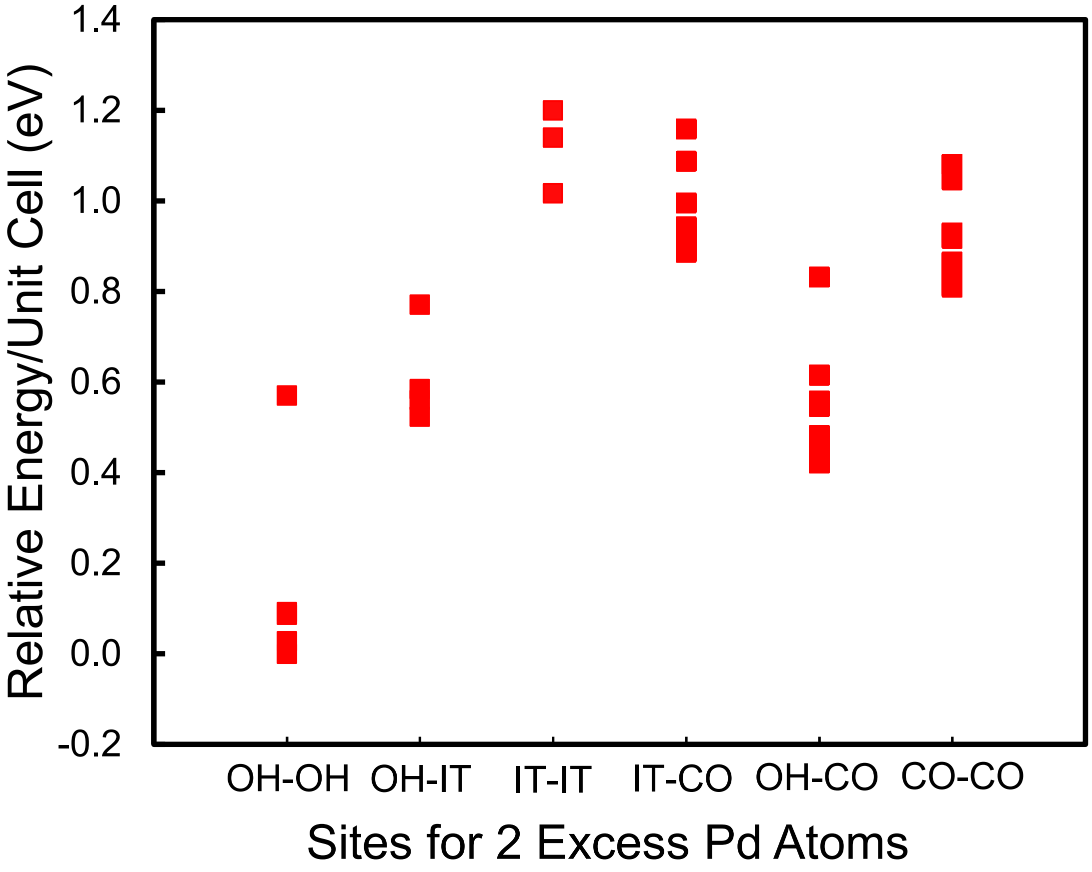

Figure S4. $Pd_{10}Zn_{42}$ bulk calculations with 8 Pd atoms in OT sites and two Pd atoms in OH-OH, OH-IT, IT-IT, IT-CO, OH-CO and CO-CO sites.

For Pd_8AuZn_{43}, Pd_8AgZn_{43} and Pd_8CuZn_{43}, the Au, Ag and Cu atom was placed in OT, OH, IT or CO sites and bulk structures were optimized. When Au, Ag and Cu was placed in OT site, the excess Pd was placed in OH site. The corresponding relative bulk energies are shown in Figure S5, Figure S6 and Figure S7. The energetically favorable structure has 8 Pd atoms in the OT sites and the Au, Ag and Cu atoms in OH sites, which agrees with XRD results.

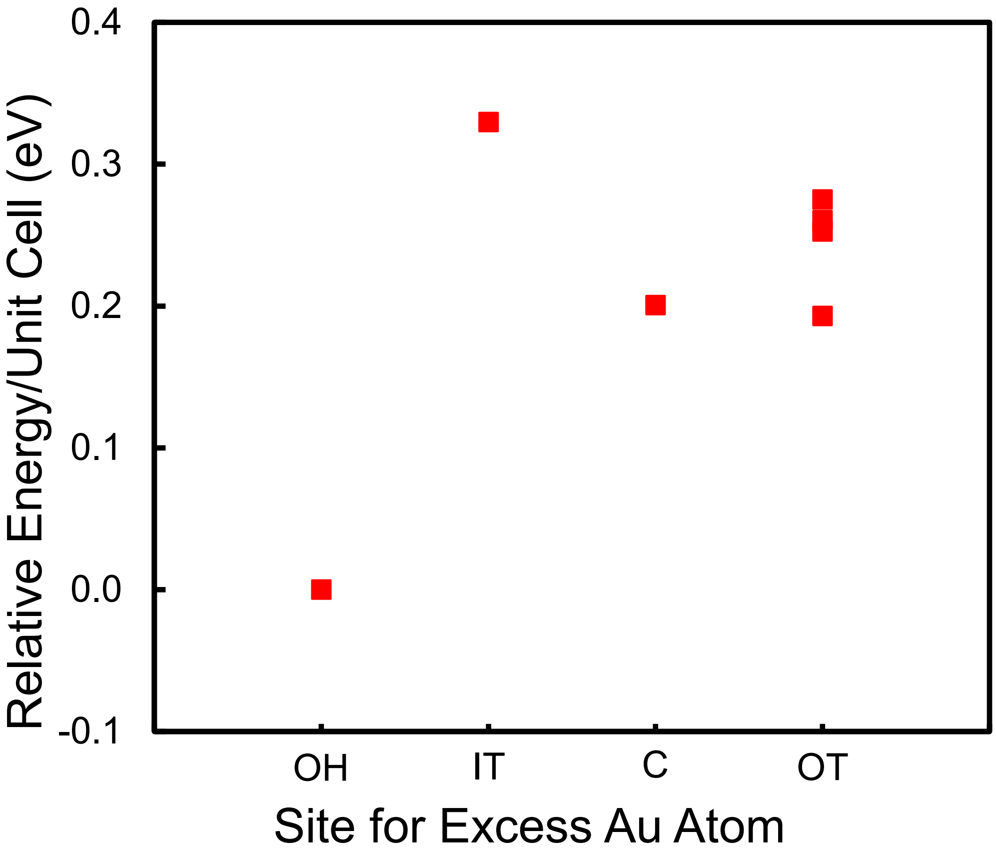

Figure S5. Pd_8AuZn_{43} bulk calculations with the Au atom in OH, IT, CO or OT sites. Pd was placed in an OH site when a Au atom was in an OT site.

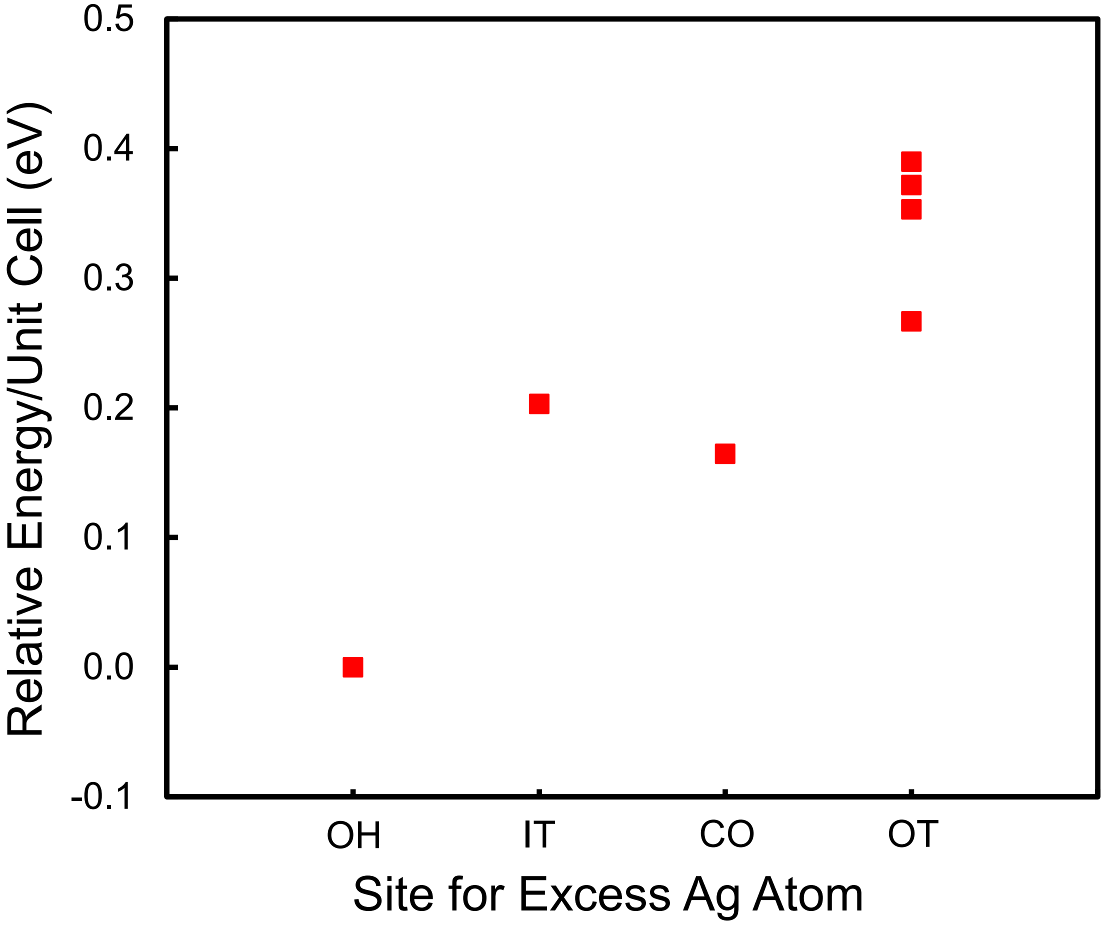

Figure S6. Pd_8AgZn_{43} bulk calculations with the Ag atom in OH, IT, CO or OT sites. Pd was placed in an OH site when a Ag atom was in an OT site.

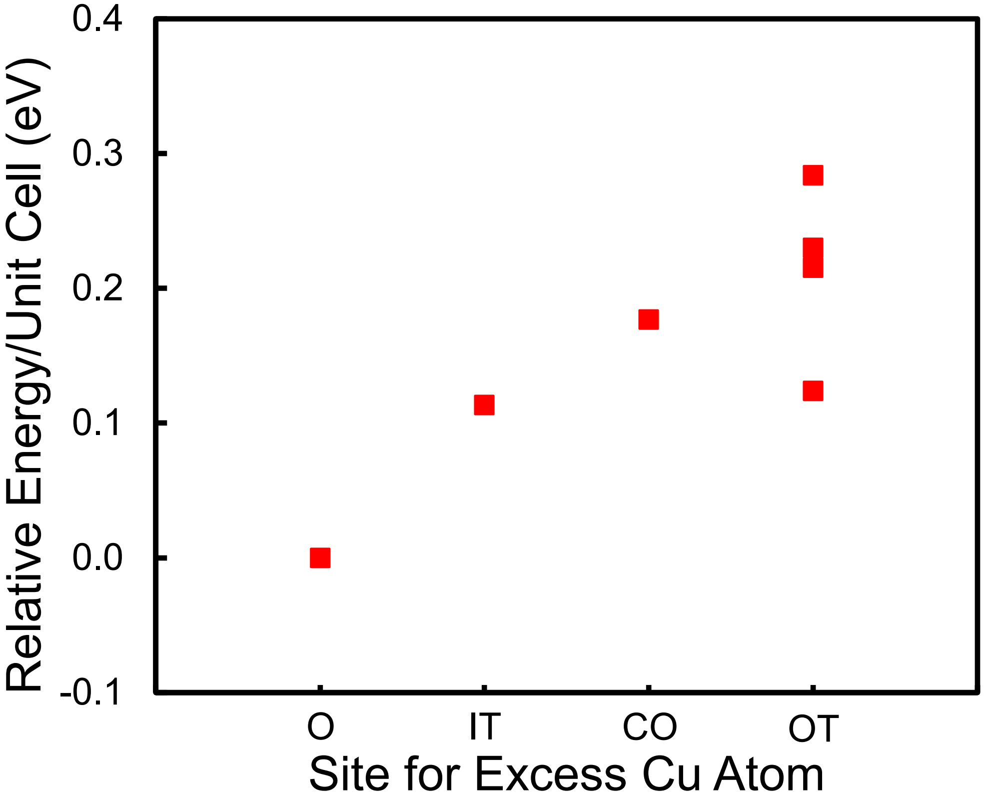

Figure S7. Pd_8CuZn_{43} bulk calculations with the Cu atom in OH, IT, CO and OT site. Pd was placed in an OH site when a Cu atom was in an OT site.

We also examined Ag and Cu atom distribution in $Pd_8Ag_3Zn_{41}$ and $Pd_8Cu_3Zn_{41}$ to match the composition of the experimental samples. We enumerated all inequivalent structures for 3Ag and 3Cu occupying OH sites and calculated the energy of each of these 9 structures. We also generated 20 different distributions that included Ag or Cu atoms in non-OH sites. The structures with all 3 Ag or all 3 Cu atoms in OH sites are significantly more stable than any other distribution considered (Figure S8 and S9). This indicates the site preference observed in $Pd_8Ag(Cu)Zn_{43}$ carries through to materials with higher Ag (Cu) concentration, as also observed with more complete distribution sampling for $Pd_{10}Zn_{42}$. The most stable $Pd_8Ag_3Zn_{41}$ and $Pd_8Cu_3Zn_{41}$ bulk structures expose Pd-Ag-Pd and Pd-Cu-Pd trimers, which are identical with the most stable surface configuration of the corresponding Pd_8AgZn_{43} and Pd_8CuZn_{43}.

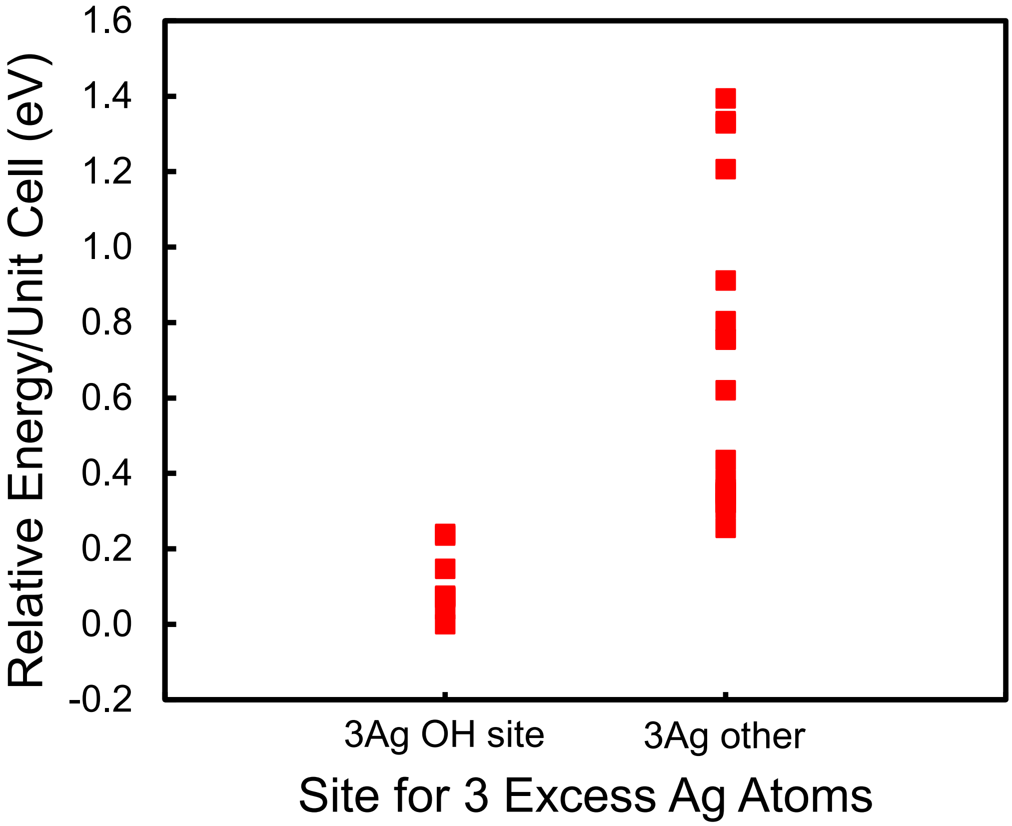

Figure S8. $Pd_8Ag_3Zn_{41}$ relative DFT energies with 3Ag in OH site (8 Pd in OT site) and 3 Ag randomly distributed to another site.

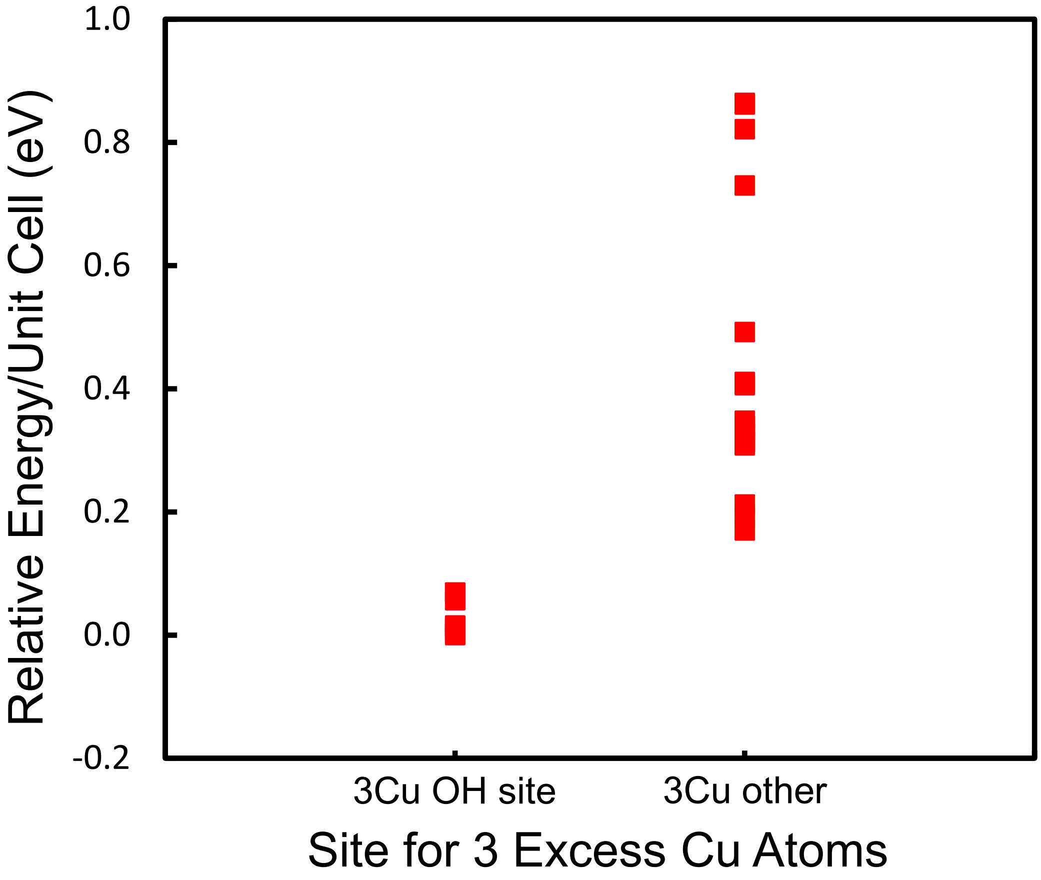

Figure S9: $Pd_8Cu_3Zn_{41}$ relative DFT energies with 3Cu in OH site (8 Pd in OT site) and 3 Cu randomly distributed to another site.

S6: Comparison of Surface Terminations in Pd_8Zn_{44}, Pd_9Zn_{43}, $Pd_{10}Zn_{42}$ and Pd_8MZn_{43} (M=Au, Ag, Cu)

For any of the bulk intermetallic catalysts examined here, particle surfaces are generated with unregulated high energy impact and attrition during ball milling. However, appropriately annealed surfaces should relax back to the thermodynamically preferred crystal structure. Here, first-principles calculations were performed to calculate surface energies of trimer-free surfaces and trimer-containing surfaces built from Pd_8Zn_{44}, Pd_9Zn_{43}, $Pd_{10}Zn_{44}$ and Pd_8MZn_{43} (M=Au, Ag, Cu). Four low index surfaces ((111), (100), (110) and $(1\bar{1}0)$) were considered (Table S4). The fractional contribution (based on surface energies) of each facet to the particle shape were obtained using Wulffmaker,[17] which is shown in Table S4. For Pd_8Zn_{44}, since 8 Pd atoms fully occupy OT site, only Pd monomers (Pd_1) are present on (110) and $(1\bar{1}0)$ facets, accounting for the whole surface area of particle. For Pd_9Zn_{43}, $Pd_{10}Zn_{42}$, Pd_8AuZn_{43}, Pd_8AgZn_{43} and Pd_8CuZn_{43}, the (110) facet has a denser amount of Pd or M monomers exposed. The $(1\bar{1}0)$ facet exposes Pd trimers (Pd_3) or Pd-M-Pd (M = Au, Ag, Cu) trimers. DFT calculations suggest both (110) and $(1\bar{1}0)$ are energetically favorable surfaces, which make up over 90% of the exposed surface area. For $Pd_{10}Zn_{42}$, the Pd monomer density on (110) surface facet increases compared with Pd_9Zn_{43}, and the trimer density increases on the $(1\bar{1}0)$ surface facet, as shown in Table S5.

Table S4. Surface energies and fraction of exposed surface in Wulff construction, for four low index surfaces ((111), (100), (110) and ($1\bar{1}0$)) of Pd_8Zn_{44}, Pd_9Zn_{43}, $Pd_{10}Zn_{42}$ and Pd_8MZn_{43} (M = Au, Ag, Cu)

Sample	Facet	Surface Energy (eV/Å^2)	Fractional exposed area
Pd_8Zn_{44}	(110)	0.060	0.50
	($1\bar{1}0$)	0.060	0.50
	(100)	0.090	0
	(111)	0.15	0
Pd_9Zn_{43}	(110)	0.060	0.45
	($1\bar{1}0$)	0.060	0.45
	(100)	0.067	0.10
	(111)	0.15	0
$Pd_{10}Zn_{42}$	(110)	0.060	0.48
	($1\bar{1}0$)	0.060	0.48
	(100)	0.070	0.04
	(111)	0.16	0
Pd_8AuZn_{43}	(110)	0.058	0.44
	($1\bar{1}0$)	0.057	0.46
	(100)	0.066	0.10

	(111)	0.15	0
Pd_8AgZn_{43}	(110)	0.060	0.46
	$(1\bar{1}0)$	0.060	0.46
	(100)	0.071	0.08
	(111)	0.15	0
Pd_8AgZn_{43}	(110)	0.061	0.46
	$(1\bar{1}0)$	0.061	0.46
	(100)	0.072	0.08
	(111)	0.15	0

Table S5. (110) and ($1\bar{1}0$) surface configurations of Pd_8Zn_{44}, Pd_9Zn_{43}, $Pd_{10}Zn_{42}$ and Pd_8MZn_{43}.

catalyst	110	$1\bar{1}0$
Pd_8Zn_{44}	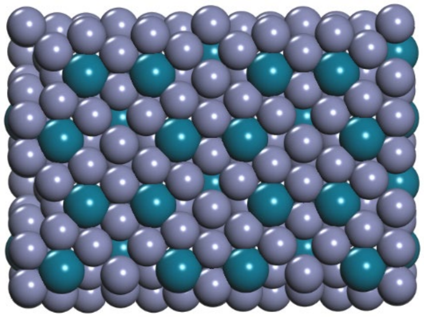	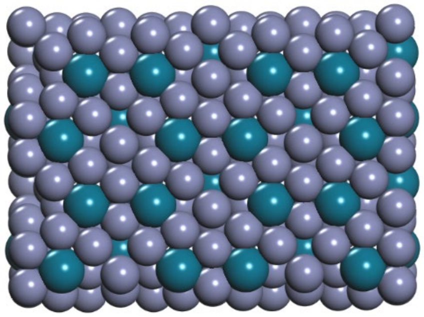
Pd_9Zn_{43}	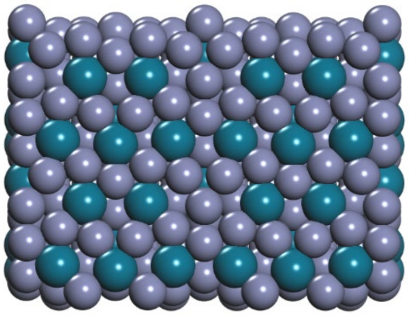	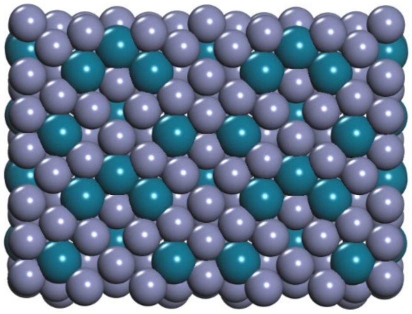
$Pd_{10}Zn_{42}$	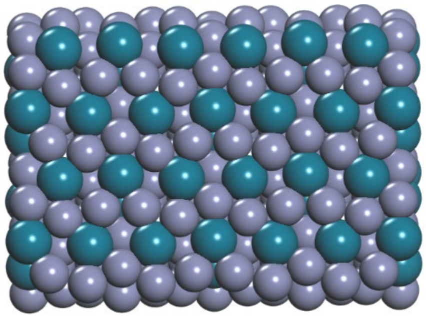	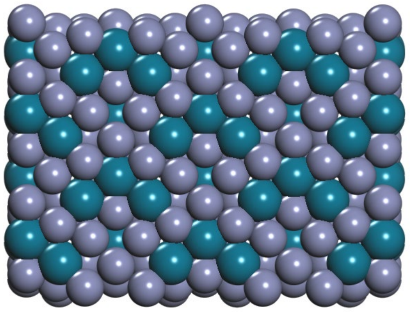
Pd_8MZn_{43} (M = Au, Ag, Cu)	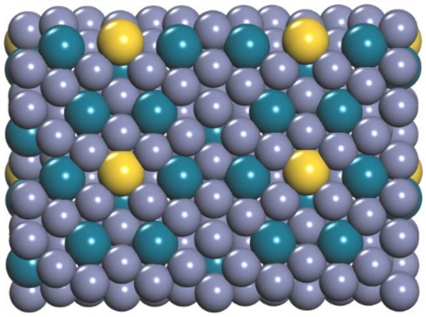	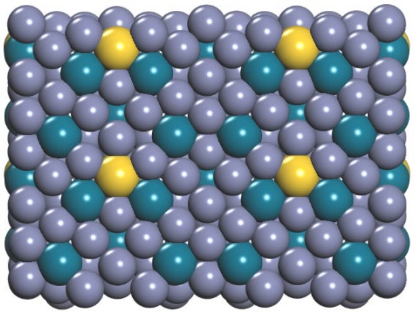

S7: Acetylene and Ethylene Adsorption on Pd Monomer, Pd Trimer and Pd-M-Pd (M = Au, Ag, Cu) Surfaces

Figure S10 shows acetylene and ethylene binding energies and adsorption configurations on Pd monomer, Pd trimer, Pd-M-Pd trimer surfaces and pure Pd (111). On Pd(111), the adsorption of acetylene is favored on a hollow site with the carbons taking on sp^3 character, while the bridge site is energetically favored for ethylene adsorption.[23-25] Acetylene binds on a Pd(111) hollow site with an adsorption energy of -1.72 eV and an elongated carbon-carbon bond (1.35 Å); ethylene binds to a Pd(111) bridge site with an adsorption energy of -0.85 eV and an elongated carbon-carbon bond of 1.45 Å. The adsorption energies and geometries agree with prior DFT results for Pd(111).[26]

The Pd_9Zn_{43} trimer site has a larger Pd-Pd-Pd angle than that about Pd(111) hollow sites, causing a difference in the adsorbed acetylene structure on the Pd_3 γ-brass sites relative to close-packed hollow sites. As shown in Figure S10, acetylene forms a π-bond with the center Pd and di-σ bond with the outer Pd atoms. A similar acetylene adsorption geometry was reported in prior computational studies for Pd_3 sites on PdGa($\bar{1}\bar{1}\bar{1}$) and Pd_3In(111) trimer sites.[27,28] Pd_3In(111) exposes Pd_3 sites, however, they are interconnected rather than being isolated by In atoms. PdGa($\bar{1}\bar{1}\bar{1}$) exposes isolated Pd_3 sites, but they have not been examined computationally or experimentally for selective hydrogenation catalysis. The adsorption energy on the Pd_9Zn_{43} trimer is weaker than on PdGa($\bar{1}\bar{1}\bar{1}$) and Pd_3In(111) trimer sites, which may be ascribed to the unique geometry of the γ-brass Pd_3 site. Our Pd trimer forms an isosceles triangle, whereas Pd_3 sites on PdGa($\bar{1}\bar{1}\bar{1}$) and Pd_3In(111) are closer to an equilateral triangle. However, the moderate acetylene adsorption energy of -0.85 eV on Pd_9Zn_{43} trimer sites does allow for activation of the C-C triple bond. Ethylene adsorption on an outer Pd atom atop position of the Pd_3 site is the energetically most favorable configuration, with a binding energy of -0.29 eV. This adsorption configuration is consistent with that reported for a PdGa ($\bar{1}\bar{1}\bar{1}$) trimer site, in which ethylene adsorbed through a π-bond with a Pd atom.

On the Pd_8Zn_{44} monomer surface, di-σ bound acetylene on two Pd monomers is the most favorable adsorption configuration, with an adsorption energy of -0.49 eV and a C-C bond length of 1.36 Å. Such adsorption geometry is in agreement with that reported for PdIn(110)[27] and PdZn $L1_0$ type (100) Pd monomer surfaces.[26] Ethylene adsorption on a monomer atop site is quite similar to ethylene binding to the Pd trimer site, with a π bond adsorption configuration and adsorption energy of -0.30 eV.

All examined surfaces include Pd-M-Pd sites where M can be Zn, Au, Ag, Cu or Pd atoms. Thus acetylene and ethylene binding geometries are similar across these sites. However, depending on the center atom of the trimer, the acetylene binding strength follows the trend of Pd (-0.85 eV) is stronger than Cu (-0.70 eV) > Zn (-0.49 eV) > Ag (-0.44eV) > Au (-0.40 eV). Ethylene, however, binds through mainly a single Pd atom and its binding energy is effectively independent of the identity of the trimer's central atom.

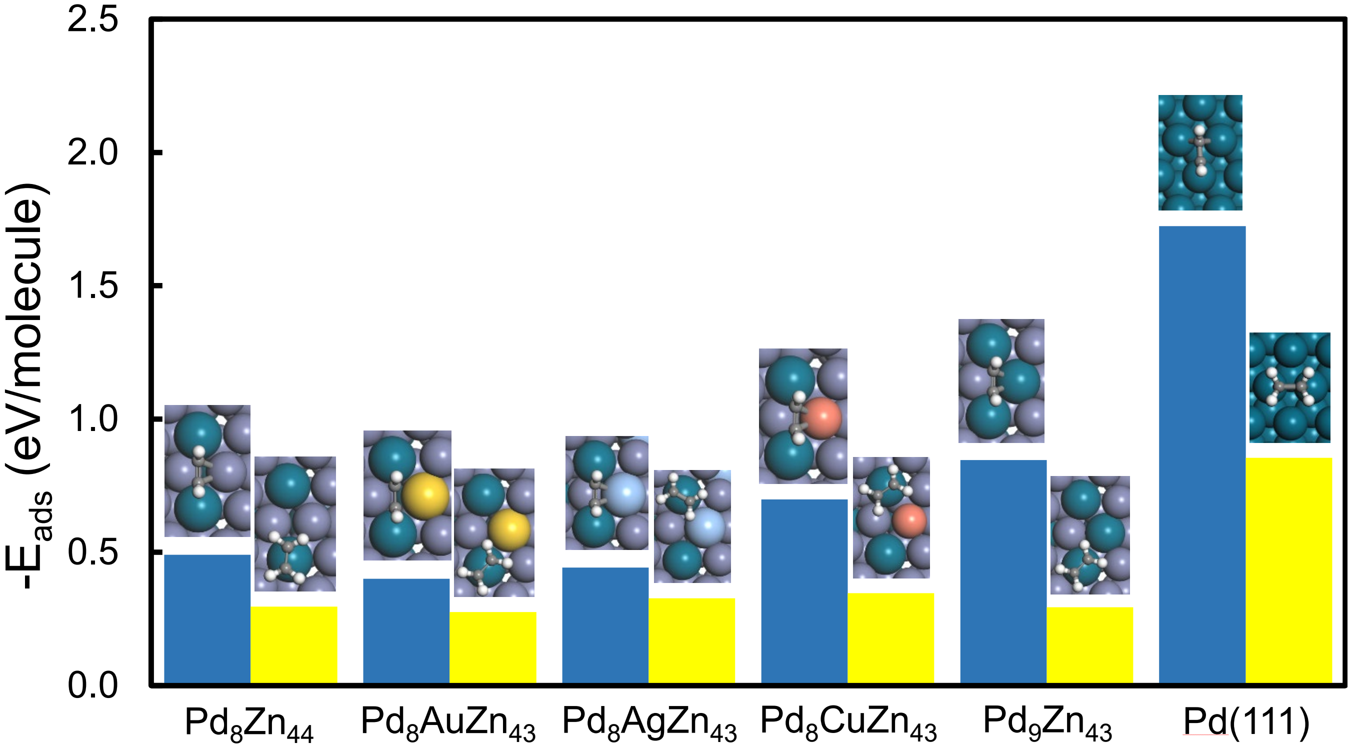

Figure S10. Acetylene (blue bars) and ethylene (yellow bars) adsorption energy and configuration on Pd_8Zn_{44}, Pd_8AuZn_{43}, Pd_8AgZn_{43}, Pd_8CuZn_{43}, Pd_9Zn_{43} and Pd (111) surfaces.

S8: Acetylene Hydrogenation Reaction Mechanism

Table S6 shows the intermediate and transition state structures involved in acetylene hydrogenation on Pd_8MZn_{43} (M = Pd, Cu, Ag, Au and Zn). Hydrogenation occurs through a step-wise mechanism. Acetylene binding on Pd-M-Pd trimer sites leaves Pd monomer sites open for H_2 dissociation. H atoms diffuse across Zn bridge sites to form a transition state structure for C-H bond formation in which both C and H share the same Pd atom. The apparent kinetic barrier for this first C-H formation step follows the trend of Pd_8Zn_{44} (0.41 eV) > Pd_8AuZn_{43} (0.34 eV) > Pd_8CuZn_{43} (0.31 eV) > Pd_8AgZn_{43} (0.30 eV) > Pd_9Zn_{43} (0.27 eV), suggesting the central atom in the Pd-M-Pd trimer impacts the acetylene hydrogenation rate.

Ethylene hydrogenation energetics are also strongly impacted by the central atom identify in the Pd-M-Pd trimer. Ethylene binds to an outer Pd of the trimer, whereas H_2 dissociates and H atoms bind to the other Pd atom across the trimer. H then diffuses across the central atom of the timer and forms the transition state for C_2H_4 hydrogenation. The apparent kinetic barrier has the order of Pd_8Zn_{44} (0.81 eV) > Pd_8AgZn_{43} (0.61 eV) > Pd_8AuZn_{43} (0.60 eV) > Pd_8CuZn_{43} (0.59 eV) > Pd_9Zn_{43} (0.40 eV).

Table S6. Acetylene hydrogenation geometric structures, C-H bond formation distance is label as red.

Catalysts	Elementary step	Reaction state		
		Initial State	Transition State	Final State
Pd_8Zn_{44}	$C_2H_2 + H = C_2H_3$	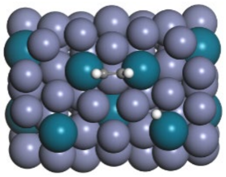	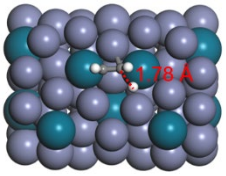	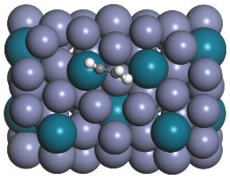
	$C_2H_3 + H = C_2H_4$	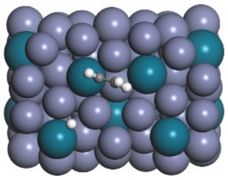	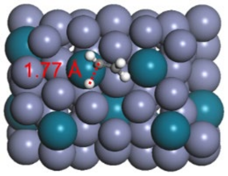	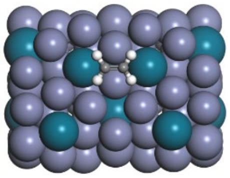
	$C_2H_4 + H = C_2H_5$	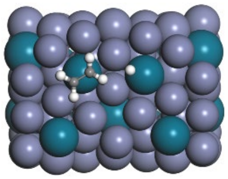	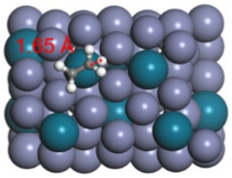	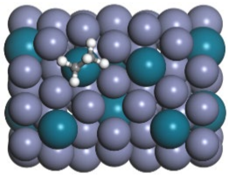
	$C_2H_5 + H = C_2H_6$	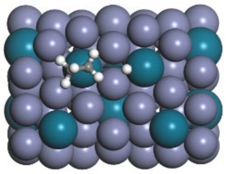	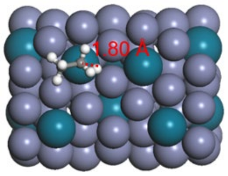	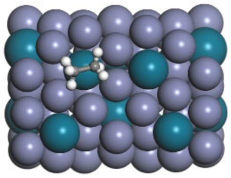
Pd_8AuZn_{43}	$C_2H_2 + H = C_2H_3$	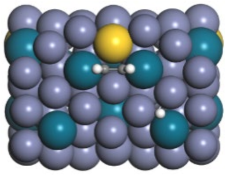	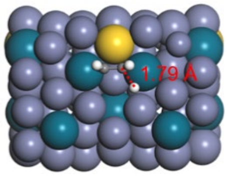	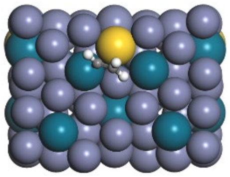
	$C_2H_3 + H = C_2H_4$	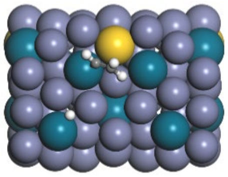	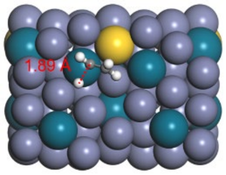	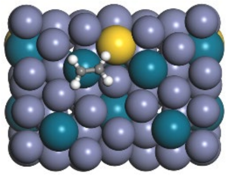
	$C_2H_4 + H = C_2H_5$	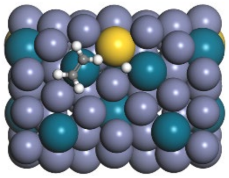	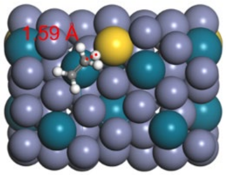	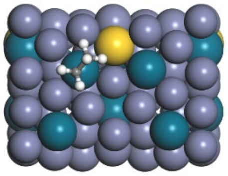

	$C_2H_5 + H = C_2H_6$	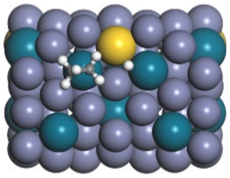	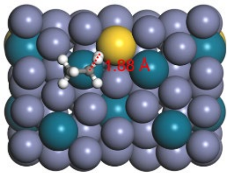	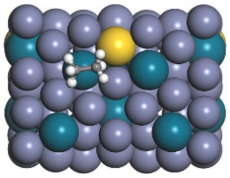
Pd_8AgZn_{43}	$C_2H_2 + H = C_2H_3$	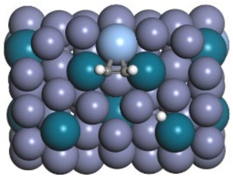	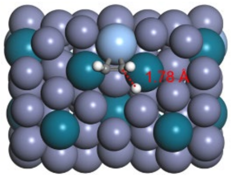	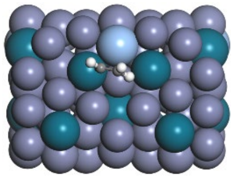
	$C_2H_3 + H = C_2H_4$	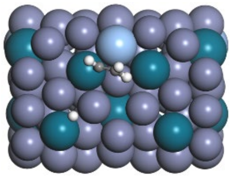	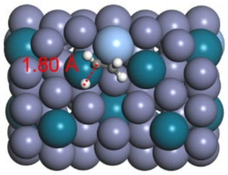	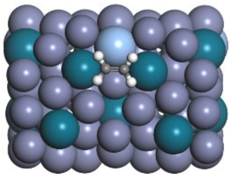
	$C_2H_4 + H = C_2H_5$	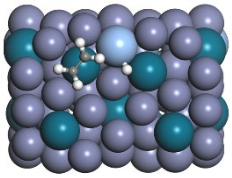	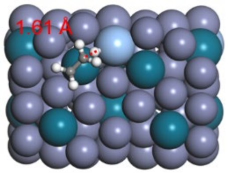	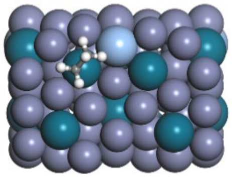
	$C_2H_5 + H = C_2H_6$	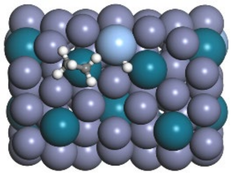	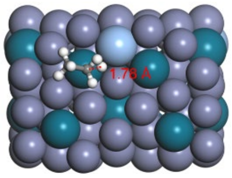	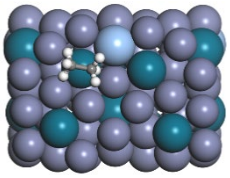
Pd_8CuZn_{43}	$C_2H_2 + H = C_2H_3$	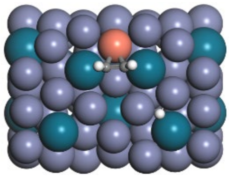	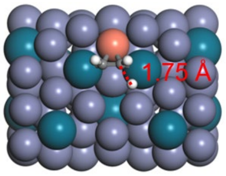	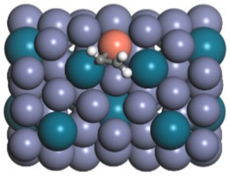
	$C_2H_3 + H = C_2H_4$	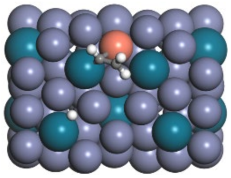	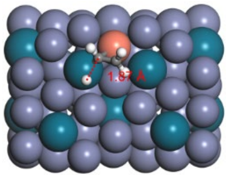	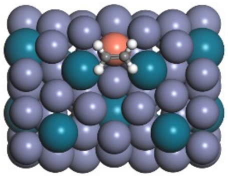
	$C_2H_4 + H = C_2H_5$	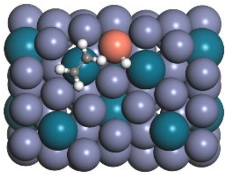	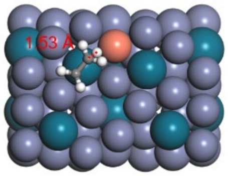	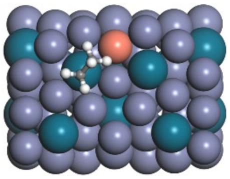

	$C_2H_5 + H = C_2H_6$	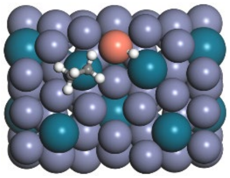	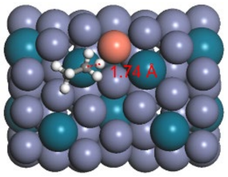	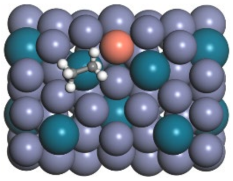
Pd_9Zn_{43}	$C_2H_2 + H = C_2H_3$	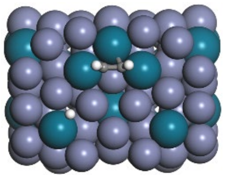	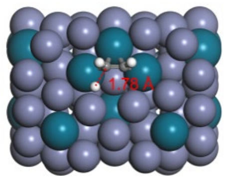	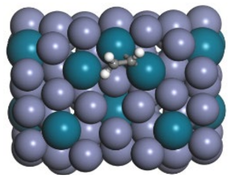
	$C_2H_3 + H = C_2H_4$	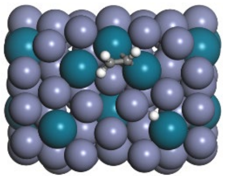	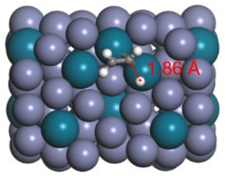	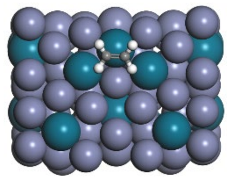
	$C_2H_4 + H = C_2H_5$	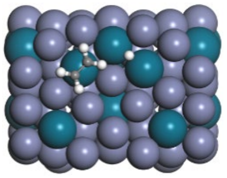	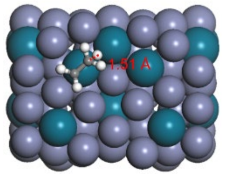	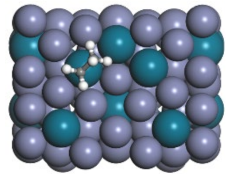
	$C_2H_5 + H = C_2H_6$	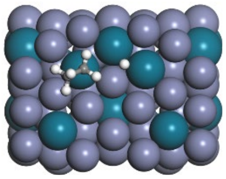	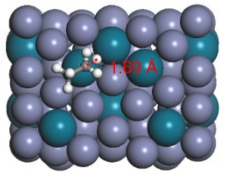	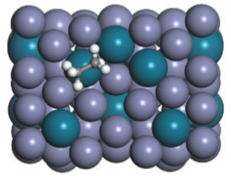

S9: Advantages of Isotope Labeling in Acetylene Semi-hydrogenation in Presence of Excess Ethylene

In this study we have opted to use two different isotopes ^{13}C and ^{12}C for ethylene and acetylene respectively as it provides two major advantages over unlabeled reactions in terms of data analysis:

1. Since ethylene is in significant excess it is typically difficult to accurately detect any increase in the ethylene signal coming from acetylene semi-hydrogenation. Borodzinski and Bond have previously strongly warned against directly measuring changes in ethylene concentration for this reaction because of difficulty in accurate quantification.[29,30] Isotope labeling provides an alternative approach to directly quantify changes in ethylene partial pressure as described in Section S1.8. Isotope labeling, typically with ^{14}C, have also been successfully applied as early as the 1970s for accurate quantification of acetylene semi-hydrogenation selectivity.[31,32] More recently, Spanjers et al.[5,10] used ^{13}C-acetylene and ^{12}C-ethylene towards this end.
2. The use of isotope labeling allows us to track the individual fates of ethylene and acetylene feed during reaction by defining an intrinsic selectivity term consistent with Leviness et al.[32] It demonstrated the intrinsic selectivity to ethylene hydrogenation remains quite high for both Pd_8Zn_{44} and Pd_9Zn_{43} (Figure 3b). The poor *net* ethylene selectivity on Pd_9Zn_{43} is a result of parallel hydrogenation of feed ethylene rather than direct or sequential full hydrogenation of acetylene. Such a conclusion could not be reached in the absence of isotope labeling.

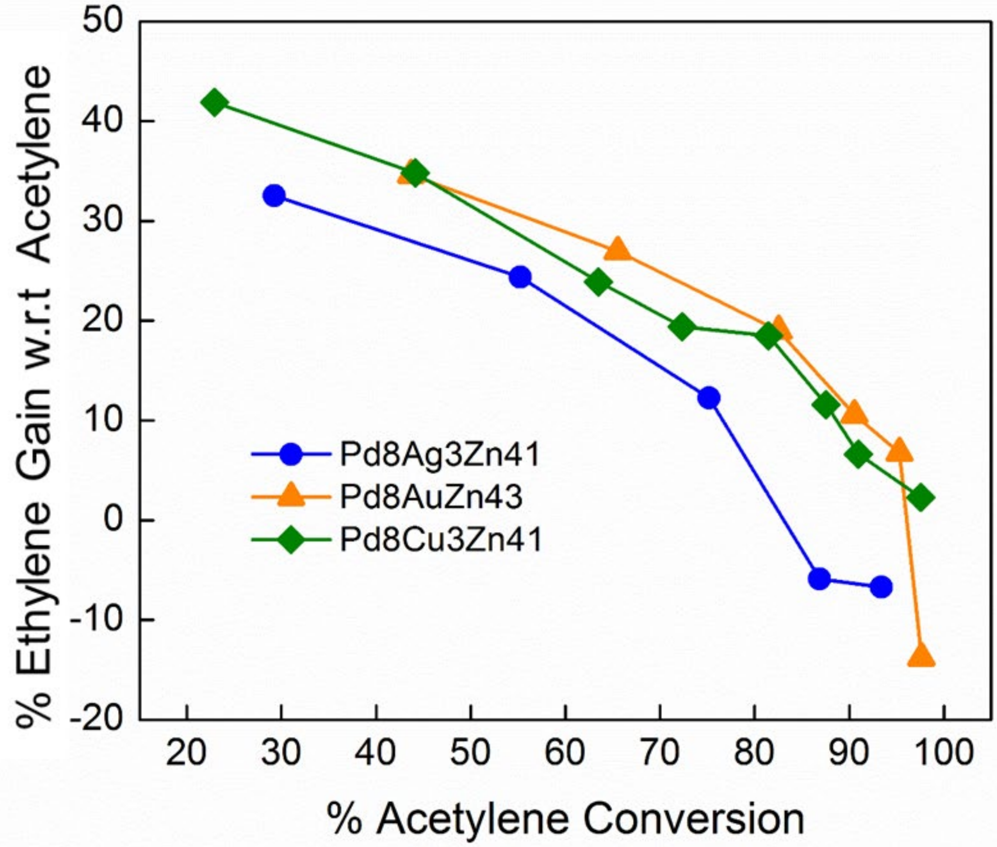

Figure S11. Net ethylene selectivity on $Pd_8Ag_3Zn_{41}$ (blue circles), Pd_8AuZn_{43} (yellow triangles) and $Pd_8Cu_3Zn_{41}$ (green diamonds) at 160°C, $C_2H_2 : C_2H_4 : H_2 = 1:31:18$.

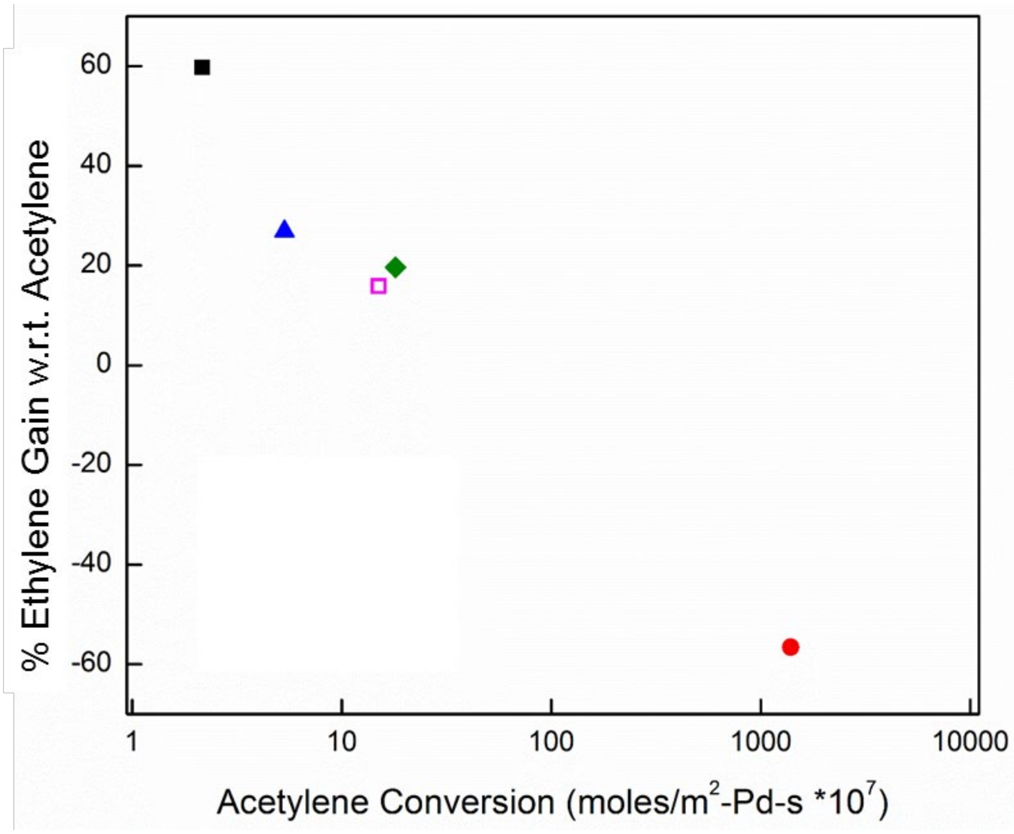

Figure S12. Average activity (acetylene conversion ~3-15%, flow reactor) and net ethylene selectivity (acetylene conversion range ~40-90%, batch reactor) on different catalysts. Black square indicates Pd_8Zn_{44}, red circle indicates Pd_9Zn_{43}, blue triangle indicates Pd_8AuZn_{43}, pink hollow square indicates $Pd_8Ag_3Zn_{41}$ and green diamond indicates $Pd_8Cu_3Zn_{41}$.

S10: DFT-based Cluster Expansion Method (CEM)

We used the cluster expansion method (CEM)[33] – a type of machine learning technique – to predict energies for the Pd-Zn intermetallic configurations of interest:

$$J = \xi^{-1} E^{ord} \tag{9}$$

$$E = \xi J \tag{10}$$

where E^{ord} is a DFT-calculated energy for ordered compounds, ξ the correlation function (i.e., a set of unique numbers to characterize a given structure)[33], ξ^{-1} the inverse or pseudo-inverse of the correlation function matrix, and J the effective cluster interaction energies (ECI's). We performed DFT calculations for 154 Pd-Zn γ-brass configurations for accurate results (E^{ord}), used the ATAT (Alloy Theoretic Automated Toolkit)[34] to estimate the values of ξ and J, and then predicted energies for all independent Pd-Zn γ-brass configurations in a sublattice discussed below.

Table S7 lists the Wyckoff positions/sites in the γ-brass structure. According to the symmetry of the γ-brass structure with space group $I\bar{4}3m$, we constructed a sublattice model of $(\mathrm{Pd,Zn})_4^{\mathrm{OT}}(\mathrm{Pd,Zn})_4^{\mathrm{IT}}(\mathrm{Pd,Zn})_6^{\mathrm{OH}}(\mathrm{Pd,Zn})_{12}^{\mathrm{CO}}$ with 26 atoms in the primitive cell of γ-brass structure to search all possible configurations with distributions of Pd and Zn atoms in the sites of IT, OT, OH and CO. Considering inequivalent symmetry, 2,831,392 independent configurations from 2^{26} possible configurations were generated; specifically, 729 independent Pd_4Zn_{22} configurations from 14,950 configurations and 2,972 independent Pd_5Zn_{21} configurations from 65,780 configurations were generated using the ATAT code.

Table S7. Wyckoff positions/sites in the γ-brass structure with space group $I\bar{4}3m$.

Site	**Wyckoff position with multiplicity and Wyckoff letter**
Inner tetrahedral (IT)	8c
Outer tetrahedral (OT)	8c
Octahedral (OH)	12e
Cubo-octahedral (CO)	24g

S11: References

1 Spanjers, C. S. *et al.* Determination of Bulk and Surface Atomic Arrangement in Ni-Zn gamma-Brass Phase at Different Ni to Zn Ratios. *Chemistry of Materials* **29**, 504-512 (2017).

2 Edstrom, V. A. & Westman, S. X-ray Determination of Structure of Cubic Gamma Pd,Zn Phase. *Acta Chemica Scandinavica* **23**, 279-285 (1969).

3 Gourdon, O. *et al.* Atomic distributions in the gamma-brass structure of the Cu-Zn system: A structural and theoretical study. *Inorganic Chemistry* **46**, 251-260 (2007).

4 Johansso.A, Ljung, H. & Westman, S. X-ray and Neutron Diffraction Studies on Gamma-Ni,Zn and Gamma-Fe,Zn. *Acta Chemica Scandinavica* **22**, 2743-2753 (1968).

5 Spanjers, C. S. *et al.* Zinc inclusion to heterogeneous nickel catalysts reduces oligomerization during the semi-hydrogenation of acetylene. *Journal of Catalysis* **316**, 164-173 (2014).

6 Vonheidenstam, O., Johansson, A. & Westman, S. A Redetermination of Distribution of Atoms in Cu_5Zn_8, Cu_5Cd_8 and Cu_9Al_4. *Acta Chemica Scandinavica* **22**, 653-661 (1968).

7 Thimmaiah, S., Crumpton, N. A. & Miller, G. J. Crystal Structures and Stabilities of gamma-and. gamma '-Brass Phases in $Pd_{2-x}Au_xZn_{11}$ ($x = 0.2$-0.8): Vacancies vs. Valence Electron Concentration. *Zeitschrift Fur Anorganische Und Allgemeine Chemie* **637**, 1992-1999 (2011).

8 Price, G. L. & Iglesia, E. Matrix-Method for Correction of Mass Spectra in Deuterium-Exchange Applications. *Industrial & Engineering Chemistry Research* **28**, 839-844 (1989).

9 Bui, L. & Bhan, A. Mechanisms for C-C bond cleavage and formation during acrolein production on a mixed metal oxide catalyst. *Applied Catalysis A-General* **546**, 87-95 (2017).

10 Spanjers, C. S., Sim, R. S., Sturgis, N. P., Kabius, B. & Rioux, R. M. In Situ Spectroscopic Characterization of $Ni_{1-x}Zn_x$/ZnO Catalysts and Their Selectivity for Acetylene Semihydrogenation in Excess Ethylene. *Acs Catalysis* **5**, 3304-3315 (2015).

11 Kresse, G. & Furthmuller, J. Efficiency of ab-initio total energy calculations for metals and semiconductors using a plane-wave basis set. *Computational Materials Science* **6**, 15-50 (1996).

12 Kresse, G. & Furthmuller, J. Efficient iterative schemes for ab initio total-energy calculations using a plane-wave basis set. *Physical Review B* **54**, 11169-11186 (1996).

13 Kresse, G. & Hafner, J. Ab Initio Molecular Dynamics for Liquid Metals. *Physical Review B* **47**, 558-561 (1993).

14 Perdew, J. P., Burke, K. & Ernzerhof, M. Generalized gradient approximation made simple. *Physical Review Letters* **77**, 3865-3868 (1996).

15 Methfessel, M. & Paxton, A. T. High Precision Sampling for Brillouin Zone Integration in Metals. *Physical Review B* **40**, 3616-3621 (1989).

16 Monkhorst, H. J. & Pack, J. D. Special Points for Brillouin Zone Integrations. *Physical Review B* **13**, 5188-5192 (1976).

17 Zucker, R. V., Chatain, D., Dahmen, U., Hagege, S. & Carter, W. C. New software tools for the calculation and display of isolated and attached interfacial-energy minimizing particle shapes. *Journal of Materials Science* **47**, 8290-8302 (2012).

18 Crosby, L., Enterkin, J., Rabuffetti, F., Poeppelmeier, K. & Marks, L. Wulff shape of strontium titanate nanocuboids. *Surface Science* **632**, L22-L25 (2015).

19 Curiotto, S. *et al.* Copper crystals on the (11-20) sapphire plane: orientation relationships, triple line ridges and interface shape equilibrium. *Journal of Materials Science* **48**, 3013-3026 (2013).

20 Li, T. & de la Cruz, M. O. Surface energy fluctuation effects in single crystals of DNA-functionalized nanoparticles. *Journal of Chemical Physics* **143**, 243156 (2015).

21 Sen, F. G. *et al.* Towards accurate prediction of catalytic activity in IrO_2 nanoclusters via first principles-based variable charge force field. *Journal of Materials Chemistry A* **3**, 18970-18982 (2015).

22 Henkelman, G. & Jonsson, H. Improved tangent estimate in the nudged elastic band method for finding minimum energy paths and saddle points. *Journal of Chemical Physics* **113**, 9978-9985 (2000).

23 Belelli, P. G., Ferullo, R. M. & Castellani, N. J. Unsaturated hydrocarbons adsorbed on low coordinated Pd surface: A periodic DFT study. *Surface Science* **604**, 386-395, (2010).

24 Mittendorfer, F., Thomazeau, C., Raybaud, P. & Toulhoat, H. Adsorption of unsaturated hydrocarbons on Pd(111) and Pt(111): A DFT study. *Journal of Physical Chemistry B* **107**, 12287-12295 (2003).

25 Pacchioni, G. & Lambert, R. M. Cyclization of Acetylene over Pd(111) - A Theoretical Study of Reaction Mechanims and Surface Intermediates. *Surface Science* **304**, 208-222 (1994).

26 Zhou, H. R. *et al.* PdZn Intermetallic Nanostructure with Pd-Zn-Pd Ensembles for Highly Active and Chemoselective Semi-Hydrogenation of Acetylene. *Acs Catalysis* **6**, 1054-1061 (2016).

27 Feng, Q. C. *et al.* Isolated Single-Atom Pd Sites in Intermetallic Nanostructures: High Catalytic Selectivity for Semihydrogenation of Alkynes. *Journal of the American Chemical Society* **139**, 7294-7301 (2017).

28 Prinz, J. *et al.* Isolated Pd Sites on the Intermetallic PdGa(111) and PdGa($\bar{1}\bar{1}\bar{1}$) Model Catalyst Surfaces. *Angewandte Chemie-International Edition* **51**, 9339-9343 (2012).

29 Borodzinki, A. Selective hydrogenation of ethyne in ethene-rich streams on palladium catalysts. Part 1. Effect of changes to the catalyst during reaction. *Catalysis Reviews-Science and Engineering* **48**, 91-144 (2006).

30 Borodzinski, A. & Bond, G. C. Selective hydrogenation of ethyne in ethene-rich streams on palladium catalysts, Part 2: Steady-state kinetics and effects of palladium particle size, carbon monoxide, and promoters. *Catalysis Reviews-Science and Engineering* **50**, 379-469 (2008).

31 Guczi, L., Lapierre, R. B., Weiss, A. H. & Biron, E. Acetylene Deuteration in the Presence of Ethylene-C-14. *Journal of Catalysis* **60**, 83-92 (1979).

32 Leviness, S., Nair, V., Weiss, A. H., Schay, Z. & Guczi, L. Acetylene Hydrogenation Selectivity Control on PdCu/Al2O3 Catalyststs. *Journal of Molecular Catalysis* **25**, 131-140 (1984).

33 Connolly, J. W. D. & Williams, A. R. Density-functional Theory Applied to Phase Transformations in Transition-metal Alloys. *Physical Review B* **27**, 5169-5172 (1983).

34 van de Walle, A. Multicomponent multisublattice alloys, nonconfigurational entropy and other additions to the Alloy Theoretic Automated Toolkit. *Calphad-Computer Coupling of Phase Diagrams and Thermochemistry* **33**, 266-278 (2009).